Asian Journal of Chemistry; Vol. 35, No. 8 (2023), 1781-1787

ASIAN JOURNAL OF CHEMISTRY

https://doi.org/10.14233/ajchem.2023.27807

Exploring the Decreasing Coercivity Properties of Aluminum Cobalt Ferrites Prepared by Coprecipitation Method

R. POONGODI[1], S. SENGUTTUVAN[1,*] and R. SAGAYARAJ[2,*]

[1]PG & Research Department of Chemistry, Thiru.Vi.Ka. Government Arts College (Affiliated to Bharathidasan University), Thiruvarur-610003, India
[2]PG & Research Department of Physics, St. Joseph's College of Arts and Science (Autonomous) (Affiliated to Annamalai University), Cuddalore-607001, India

*Corresponding authors: E-mail: senguttuvanathan@gmail.com; sagayarajnancy@gmail.com

Received: 29 March 2023; *Accepted*: 18 May 2023; *Published online*: 31 July 2023; AJC-21307

Cobalt aluminum ferrites were synthesized by coprecipitation method at 1000 ºC. XRD studies pointed out the employed samples ($Fe^{2+}Al_2^{3+}O_4^{2-}$, $Fe_{0.25}Co_{0.75}Al_2O_4$ and $Fe_{0.75}Co_{0.25}Al_2O_4$) were crystallized in a single phase cubic spinel form. The synthesized samples were calculated structural parameters such as crystallitesize (D: 17 nm), X-ray density (D_x: 3.97 to 4.15 g/cm^3), volume of the unit cell (V: 583.64 to 586.58 Å), lattice strain (ε: 6.9×10^{-3}), dislocation density (δ: 3.3×10^{-3}) and lattice constant (a: 8.357 to 8.371 Å). The FE-SEM microstructure confirmed that various concentrations result in different particle sizes (5 µm to 500 nm). The magnetic characteristics were investigated by VSM and magnetic parameters like saturation magnetization (M_s: 4.82×10^{-3} to 0.673 emu/g), retentivity (M_r: 1.545×10^{-3} to 0.229 emu/g), coercivity (H_c: 775.45 to 2212.8 Oe), magnetic moment (μ_B: 1.57×10^{-4} to 2.108×10^{-2}), remnant ratio (R: 0.32 to 0.357 no unit) and anisotropy constant (K: 3.418 to 177.57 J/m^3) were calculated. High coercivity materials are ideal for use in magnetic recording media, permanent magnets and microwave devices since they possess a high degree of resistance to an external magnetic force.

Keywords: Ferrites, Impedance, Coercivity, Magnetization, Coprecipitation method, Cobalt aluminum ferrites.

INTRODUCTION

The nano-revolution has had far-reaching consequences, from improved medical care to the emergence of brand-new materials and technology. Nanotechnology has enabled us to create smaller, faster and more efficient devices, as well as new materials with unique properties. It also opened up new possibilities in fields such as energy, computing and robotics. Generally, magnetic materials are classified as diamagnetic, paramagnetic and ferromagnetic. Since the discovery of a new type of super paramagnetic, the nano-revolution can be considered to have begun. These can be called nano-sized nanoferrites [1,2]. A ferrite core is a type of magnetic core made of ferrite, a sintered form of ceramic composed of iron oxide and other metal oxides. There are a number of uses for ferrite cores, ranging from antennas, biomedical sensors and magnetic cell separation to gas detectors, tissue repair and biomedicine electronics. Ferrite cores can be used for hyperthermia radiation, catalysis, magnetic drug delivery, catalytic electrodes, ferrofluids, magnetic resonance imaging (MRI) contrast development, magnetic refrigeration, memory storage devices, microwave attractors, permanent magnets, solar energy conversion, recording heads, magnetic recording, transformer cores, high-frequency electrical equipment and hard disk recording media [3,4]. All of the above uses particle size, dopant concentration, electrical properties and magnetic properties, which have a large effect on the properties of nanoferrites.

Research is being conducted on nanoferrites to create materials with specific electrical and magnetic properties, as well as tailored particle size, for targeted applications. This provides a range of benefits, such as improved energy efficiency, enhanced performance and improved reliability [5-9]. The A plane is typically composed of a metal oxide, such as iron oxide (FeO), while the B plane is composed of a different metal oxide, such as zinc oxide (ZnO). The two metal oxides are combined in a ratio of two atoms of A to four atoms of B, forming a lattice structure. The spinel ferrite structure is composed of a network of tetrahedral, with each tetrahedron consis-

ting of two A atoms and four B atoms. The metal ions in the A plane are typically arranged in a cubic arrangement, while the metal ions in the B plane are arranged in an octahedral arrangement. This arrangement of metal ions gives the spinel ferrite (AB_2O_4) its unique magnetic properties [10]. Three types of spinels are obtained depending on the distribution of ions between two distinct crystal planes. They are normal spinal structure, inverted spinal structure and partial inverted structure. A normal spinel structure is one wherein the A-site is occupied entirely by divalent ions and the B-site by trivalent ions. Conversely, an inverse spinel structure is formed when the tetrahedral sites are filled with trivalent ions. For example is cobalt ferrite ($CoFe_2O_4$) [11]. $CoFe_2O_4$ is an inverse spinel oxide, with Co^{2+} ions on B sites and Fe^{3+} ions distributed between A and B sites. The magnetic interaction in this ferrite is due to the presence of magnetic ions on the octahedral (B) site, which interact with each other through the antiferromagnetic B–O–B interaction. This interaction is responsible for the ferrimagnetic behaviour of the ferrite. The lack of magnetic ions on the A site prevents the formation of A–O–B interaction, which is necessary for antiferromagnetic interactions. The result is that the magnetic interaction in this ferrite is limited to the B site, where magnetic ions interact with each other through the antiferromagnetic B–O–B interaction [12,13]. This cobalt ferrite has high coercivity makes it ideal for use in high-frequency applications, such as in the production of high-frequency transformers and inductors. Its high mechanical hardness makes it suitable for use in abrasive applications, such as grinding and polishing. Its chemical stability makes it suitable for use in a variety of chemical processes, such as electroplating and electrochemical etching [14].

The substitution of Al^{3+} ions for Fe^{3+} ions in the B-site of ferrites results in a decrease in the saturation magnetization and coercivity. This is because Al^{3+} ions are non-magnetic and thus reduce the number of magnetic ions in the lattice. The substitution also affects the electrical properties of the ferrite, such as the dielectric constant and the electrical resistivity. This is because the Al^{3+} ions are larger than the Fe^{3+} ions, resulting in a decrease in the number of cations in the lattice and thus a decrease in the dielectric constant and electrical resistivity. The substitution of Al^{3+} ions also affects the magnetic properties of the ferrite, such as the permeability and the hysteresis loop. This is because the Al^{3+} ions are non-magnetic and thus reduce the number of magnetic ions in the lattice, resulting in a decrease in the permeability and a decrease in the hysteresis loop [15,16]. The net magnetization and the calcination temperature of aluminum (Al^{3+}) substituted cobalt ferrites decreases when Al content is increased. Bulk materials of such ferrites are affected by these changes [17]. Using various synthesizes techniques can yield different bulk and nano sizes, which can affect the cation distribution and magnetic properties. For example, different techniques can lead to different cation distributions, which can affect the magnetic properties of the material. Additionally, different sizes can also affect the magnetic properties, as smaller particles can have different magnetic properties than larger particles. This is due to the fact that smaller particles have a higher surface-to-volume ratio, which can lead to different magnetic properties. Finally, different synthesizes techniques can also affect the magnetic properties by changing the structure of the material, which can lead to different magnetic properties [18].

$FeAl_2O_4$ is a normal spinel structure, which means that the Fe^{2+} ions are tetrahedral coordinated by Al^{3+} ions and the Al^{3+} ions are octahedral coordinated by O^{2-} ions. This structure obeys the Vegard's law, which states that the lattice parameters of a solid solution are linearly related to the composition of the solution. $AlFe_2O_4$ is an inverse spinel structure, which means that the Fe^{3+} ions are tetrahedral coordinated by Fe^{2+} and Al^{3+} ions are octahedral coordinated by O^{2-} ions. This structure also obeys the Vegard's law, which states that the lattice parameters of a solid solution are linearly related to the composition of the solution [19]. When the saturation magnetization decreases caused decreasing the particle size [20,21]. And the coercivity gradually increases with decreasing particle size, a critical value representing a single domain particle. This type exhibits a superparamagnetic phase for very small particle sizes [22]. In this study, $AlFe_2O_4$ nanoferrite based on cobalt deficiency and cobalt excess are described. A hysteresis loop reveals ferro or ferrimagnetic for big (bulk) nanoparticles. Almost hysteresis loop free behaviour in small sizes and superparamagnetic behaviour in nanoparticles of the tiniest sizes [23]. The pH value to 11 is adjusted to prepare these particles and then obtained three samples using cobalt deficient concentrations and cobalt excess concentrations to obtain different crystallite sizes. Present results clearly demonstrate the possibility of adjusting/modifying the structural and magnetic properties of $Fe^{2+}Al_2^{3+}O_4^{2-}$, $Fe_{0.25}Co_{0.75}Al_2O_4$ and $Fe_{0.75}Co_{0.25}Al_2O_4$.

EXPERIMENTAL

Polyvinyl pyrrolidone (PVP) coated pure and cobalt doped aluminum ferrite nanoparticles were synthesized by chemical co-precipitation method according to the following procedure. In brief, ferric sulfate, cobalt sulfate, aluminum oxide and polyvinyl pyrrolidone (PVP) have been used to synthesize nanocrystalline ferrite samples. Ferric sulphate, cobalt sulphate and aluminum oxide 1:2 stoichiometric ratio of 100 mL of distilled water solutions was added to a 250 mL conical flask. Polyvinyl pyrrolidone was added to this mixture to prevent aggregation of particles, which acts as capping agents to some extent [24]. The mixtures were subjected to vigorous mechanical stirring for 3 h at room temperature. Meanwhile ammonia solution was added dropwise with stirring, which turns the mixture into black. The mixture was maintained at pH 11, *i.e.* the pH level was maintained for the purpose of creating a high electron capture surface [25]. The precipitate was washed 3 times with distilled water and ethanol solution separately using a centrifuge. Thus, the process was repeated three times consecutively to remove excess amine molecules and impurities. The washed precipitates were then dried in a hot air oven at 100 ºC for 6 h. After drying a black powder of cobalt doped $AlFe_2O_4$ is obtained. The dried black powder was annealed by placing it in a muffle furnace at 1000 ºC for 6 h. At the end, pure and mixed ferrite nano-samples were obtained.

RESULTS AND DISCUSSION

X-ray diffraction analysis: The X-ray diffraction patterns of $Fe_{0.25}Co_{0.75}Al_2O_4$ and $Fe_{0.75}Co_{0.25}Al_2O_4$ composite ferrites with cobalt-deficient concentrations and cobalt-excessive concentrations are shown in Fig. 1 in comparison to pure $Fe^{2+}Al_2^{3+}O_4^{2-}$ (hercynite). The crystallite size (D), X-ray density (D_x), unit cell volume (V), lattice strain (ε), dislocation density (δ), lattice constant were obtained using the primary diffraction peaks (311) for all the samples and tabulated in Table-1. All samples were confirmed ($FeAl_2O_4$ (#07-0068); Al_2O_3 (86-1410); Fe_3O_4 (#65-3107)) to conform to the *Fd*-3*m* space group, thus having single-phase properties and to be composed of face-centered cubic (FCC) [2]. From the width of the XRD peaks, an average crystallite size (D) was obtained using the Debye-Scherrer's formula [26]:

$$\text{Crystallite size (D, nm)} = \frac{0.9\lambda}{\beta\cos\theta}$$

$$\text{Lattice constant (a, Å)} = [d^2(h^2+k^2+l^2]$$

$$\text{X-ray density } (D_x, \text{ g/cm}^3) = \frac{8M}{Na^3}$$

$$\text{Unit cell volume (V, [Å]}^3) = a^3$$

$$\text{Lattice strain } (\varepsilon) = \frac{\beta\cos\theta}{4}$$

where β is the full-width half-maximum (FWHM), λ is the wavelength of the used X-ray beam, θ is the diffracting angle. The results clearly revealed that the diffraction angle of $AlFe_2O_4$ is 35.63°. The diffraction angle of $Fe_{0.25}Co_{0.75}Al_2O_4$ at cobalt-excess concentrations is 35.55°. Diffraction angle is 35.63° as the cobalt concentrations are low. It can be seen that cobalt concentrations do not affect the diffraction angle to a great extent. Thus, the crystallite size remains unchanged (D = 17 nm) and Co^{2+} does not affect the diffraction peaks. This reflects the single phase properties of crystallinity, *i.e.* magnetic single domain becomes possible. And also the crystallite optimum size is possible that the synthesis process used for the samples was adjusted in such a way as to achieve a uniform crystallite size regardless of the composition and concentration of each sample. The method of synthesis, reaction temperature and time, amount of precipitate used and other factors may have played a role in producing the same crystallite size. Also unit cell volume (V), lattice strain (ε) and lattice constant data are confirmed to strengthen above said point (Table-1). But the difference in X-ray density (D_x) is due to the very small difference in diffraction angle 8° between $Fe^{2+}Al_2^{3+}O_4^{2-}$ and $Fe_{0.25}Co_{0.75}Al_2O_4$.

Morphological studies: The crystalline structures of $Fe^{2+}Al_2^{3+}O_4^{2-}$ and $Fe_{0.25}Co_{0.75}Al_2O_4$ nanoparticles composite were characterized by FE-SEM technique. It has provides information about morphological characteristics such as micro and nanoparticles size, shape or nature of particles and different size distribution. Fig. 2 presents the FE-SEM images of the synthesized undoped and doped samples at a resolution of 500 nm and 5 µm. The FE-SEM images revealed a non-uniform, sponge-like morphology with a large number of pores, likely due to the immiscibility of aluminum, cobalt and iron. Doped

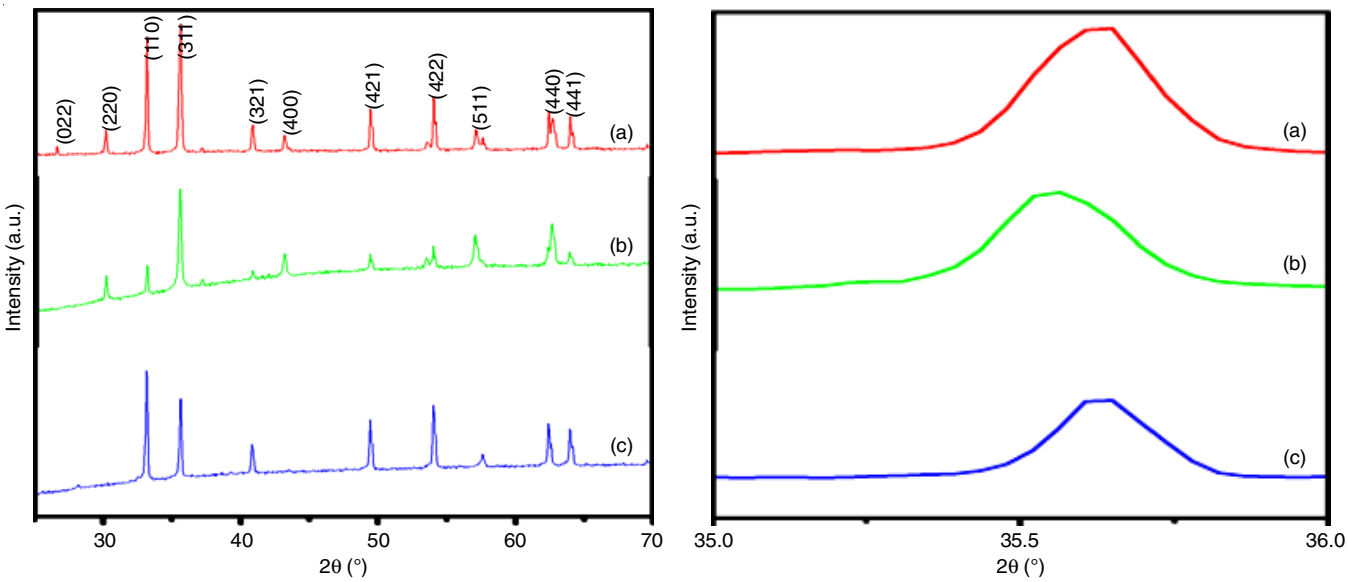

Fig. 1. X-ray diffraction of ferrite nanoparticles (a) $FeAl_2O_4$; (b) $Fe_{0.25}Co_{0.75}Al_2O_4$; (c) $Fe_{0.75}Co_{0.25}Al_2O_4$

TABLE-1
CRYSTALLITE PARAMETERS OF PURE, COBALT EXCESS AND COBALT DEFICIENCY FOR SYNTHESIZED MATERIALS

Sample	2θ (°)	D (nm)	D_x (g/cm^3)	V (Å)	a (Å)	$\varepsilon \times 10^{-3}$	$\delta \times 10^{-3}$
$FeAl_2O_4$	35.63	17	4.15	583.64	8.357	6.9	3.3
$Fe_{0.25}Co_{0.75}Al_2O_4$	35.55	17	3.97	586.58	8.371	6.9	3.3
$Fe_{0.75}Co_{0.25}Al_2O_4$	35.63	17	3.99	584.48	8.361	6.9	3.3

Crystalline size (D); X-ray density (D_x); Volume of the unit cell (V), Lattice strain (ε); Dislocation density (δ); Lattice constant (a)

samples show a less uniform pattern compared to undoped samples, indicating that the samples are not in a well-ordered form. Further from Fig. 2, it can be observed that the pore slightly decreases upon doping of Co^{2+} in $Fe^{2+}Al_2^{3+}O_4^{2-}$ [27-29]. Co, Fe, Al and O were confirmed to be exiting the sample using an EDAX spectrum (Fig. 3), which provided information about the composition of the sample. This is done by looking at the peaks in the spectrum and comparing them to known elements and compounds. Additionally, the shape of the peaks can provide information about the size and distribution of the particles in the sample. This information can be used to identify the materials present in the sample and to understand the structure and properties of the sample.

Impedance analysis: Analysis of internal resistance-affecting elements is becoming increasingly important in technology today. This is because the internal resistance of a device or circuit can have a significant impact on its performance (internal resistance of a battery). The plot shows (Fig. 4) that the impedance values decrease with increasing frequency and concentration. This is because the higher the frequency, the more energy is required to pass through the material and the higher the concentration, the more resistance the material has to the flow of energy. This is why the impedance values decrease with increasing frequency and concentration. The first two zones, limited to frequencies below 109 kHz and the second beginning at 84 kHz, are due to the fact that the material has different properties at different frequencies. At lower frequencies, the material is more conductive, allowing more energy to pass through it, while at higher frequencies; the material is less conductive, resulting in lower impedance values [30]. At higher frequencies, the presence of a space charge zone is lessened and the impedance of the material is reduced. This is due to

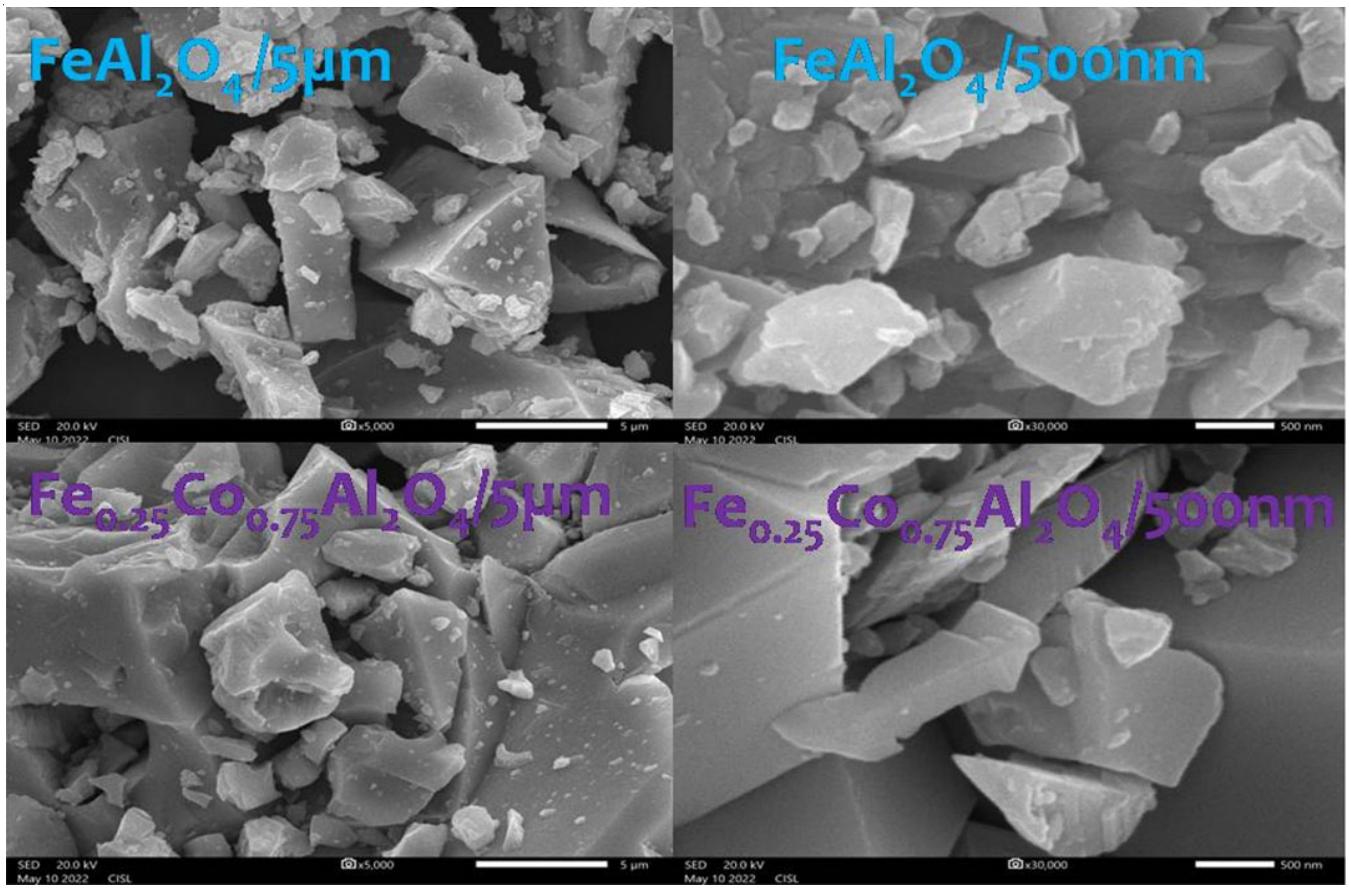

Fig. 2. FE-SEM morphology of doped and undoped ferrite nanoparticles at a resolution of 500 nm and 5 µm

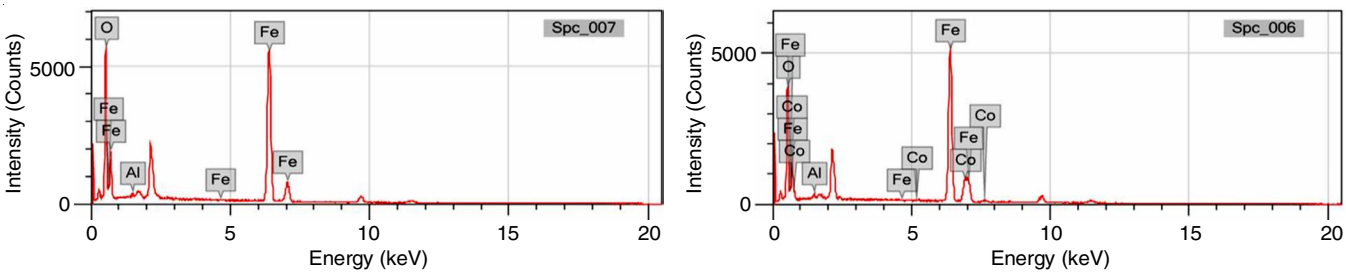

Fig. 3. EDAX spectrum of ferrite nanoparticles

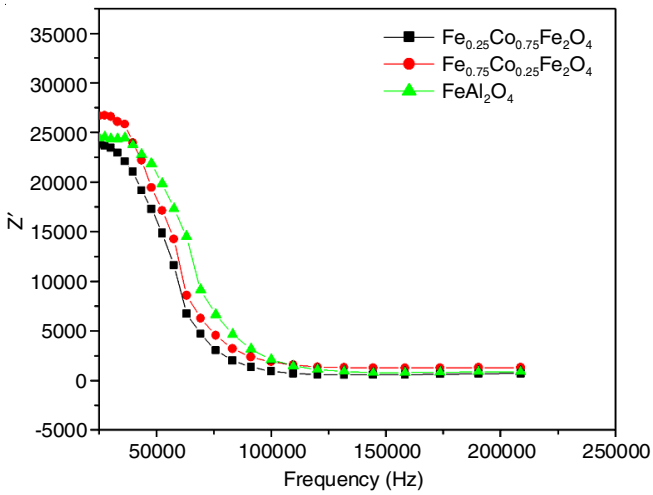

Fig. 4. Variation of real part of impedance (Z′) and frequency at zinc concentrations

the fact that the charge carriers are able to move more freely, resulting in a decrease in resistance. Additionally, the presence of a space charge zone can be used to explain the impedance of the material at lower frequencies. This is because the charge barrier is lowered by zinc concentrations, resulting in a buildup of charge carriers at grain boundaries. This buildup of charge carriers creates an active interface, which increases the impedance of the material. As a result, constant values for Z′ at various concentrations at low frequencies are observed [31,32].

Fig. 5 displays the variation of frequency-dependent Z″ at concentrations of 0.25 and 0.75. At higher concentrations, the peak shifts to higher frequencies (58 kHz), indicating that the relaxation process is faster. This is due to the increased number of grain boundaries, which increases the rate of relaxation. The peak at lower frequencies (52 kHz) is due to the presence of grain boundaries, which are responsible for the slower relaxation process. As the concentration increases, the number of grain boundaries increases, resulting in a shift of the peak to higher frequencies. This shift is due to the increased number of grain boundaries, which increases the rate of relaxation [33,34]. This impedance pattern is consistent with the

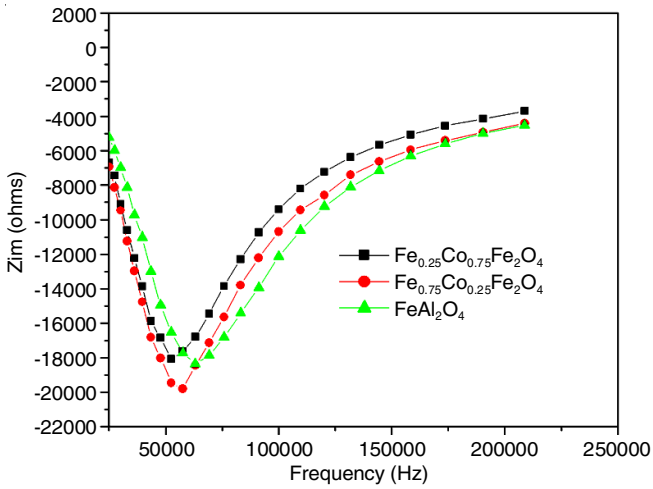

Fig. 5. Variation of imaginary part of impedance (Z″) and frequency of Zn-doped $MnFe_2O_4$

semiconducting behaviour of zinc ferrites, which suggests that charge carriers are thermally activated and accumulate at grain boundaries. This is due to the presence of defects in the crystal structure, which act as charge traps and reduce the mobility of charge carriers. The accumulation of charge carriers at grain boundaries increases the resistance of the material, resulting in the observed impedance pattern.

Magnetic properties: The M-H loops (also known as hysteresis loops) are graphical representations of the relationship between magnetization (M) and applied magnetic field (H) in a ferromagnetic and ferrimagnetic material. The shape of the M-H loop is used to characterize the magnetic properties of a material, such as its coercivity, remanence and saturation magnetization. Fig. 6 shows the magnetization curves of $FeAl_2O_4$ (FA), $Fe_{0.25}Co_{0.75}Al_2O_4$ (FCA) and $Fe_{0.75}Co_{0.25}Al_2O_4$ (FCOA) nanoparticles at room temperature. The hysteresis loops and net magnetization of the synthesized samples were measured using a vibrating sample magnetometer (VSM), with a maximum field of 2T at room temperature. The results, shown in Fig. 6, reveal that all samples have a well-saturated M-H loop. Additionally, values for saturation magnetization (M_s), remanent magnetization (M_r), coercivity (H_c), remanent ratio (R), magnetic moment (μ) and anisotropy constant (K) are listed in Table-2. Fig. 6 shows a typical magnetization curve for ferromagnetic or ferrimagnetic [21]. Iron-aluminum spinels of AB_2O_4 are classified as either "normal" or "inverse" depending on the distribution of A^{2+} and B^{3+} cations throughout the lattice. In a normal spinel, the tetrahedral sites are occupied by A^{2+} cations and octahedral sites are occupied by B^{3+} cations. An inverse spinel has A^{2+} and half of B^{3+} occupying the octahedral sites, while the other half of B^{3+} is located in the tetrahedral sites. This structure can be expressed as $(Al^{3+}\text{-}Fe^{2+}\text{-}Fe^{3+})1(Al^{3+}\text{-}Fe^{2+}\text{-}Fe^{3+})_2O_4$ [19]. $FeAl_2O_4$ is a normal spinel structure, which has oxygen atoms forming a cubic lattice, with iron and aluminum occupying octahedral and tetrahedral sites respectively. The ratio of iron to aluminum atoms is 1:2, with the iron atoms occupying octahedral sites and the aluminum atoms occupying tetrahedral sites. Conversely, inverse spinel structures have the same arrangement of atoms, but with the ratio of aluminum to iron atoms reversed, so that the aluminum atoms occupy octahedral sites and the iron atoms occupy tetrahedral sites [35,36]. $Fe_{0.25}Co_{0.75}Al_2O_4$, $Fe_{0.75}Co_{0.25}Al_2O_4$ is an inverse spinel structure. This is because the cations are arranged in an inverse spinel structure, with the Fe and Co cations occupying the octahedral sites and the Al cations occupying the tetrahedral sites. The inverse spinel structure is characterized by a higher degree of cation ordering than the normal spinel structure, which is more disordered. This higher degree of cation ordering gives the inverse spinel structure a higher degree of stability than the normal spinel structure [37-39]. From figure, it is observed that $FeAl_2O_4$ exhibit ferromagnetic properties as compared doped sample such as FCA and FCOA. It well shaped fine M-H loops, exhibits ferromagnetic properties. But doped samples were exhibits ferrimagnetic properties. This is possible when Co^{2+} in coroneted pure $FeAl_2O_4$. The highest magnetization value exits cobalt excess ferrite ($Fe_{0.25}Co_{0.75}Fe_2O_4$) then pure ($FeAl_2O_4$) and deficiency cobalt ($Fe_{0.75}Co_{0.25}Fe_2O_4$) ferrite nanocrystals

TABLE-2
MAGNETIC PARAMETERS OF PURE, COBALT DEFICIENCY AND COBALT EXCESS

Sample	M_s (emu)	M_r (emu)	Hc (Oe)	μ_B (Tesla)	R	K (J/m^3)
$FeAl_2O_4$	4.82×10^{-3}	1.545×10^{-3}	2212.8	1.570×10^{-4}	0.320	3.418
$Fe_{0.25}Co_{0.75}Al_2O_4$	0.673	0.229	775.45	2.108×10^{-2}	0.340	177.57
$Fe_{0.75}Co_{0.25}Al_2O_4$	0.305	0.109	889.94	9.594×10^{-3}	0.357	97.00

Saturation magnetization (M_s), Retentivity (M_r), Coercivity (H_c), Magnetic moment (μ_B), Remnant ratio (R), Anisotropy constant (K) and Energy product (E_p)

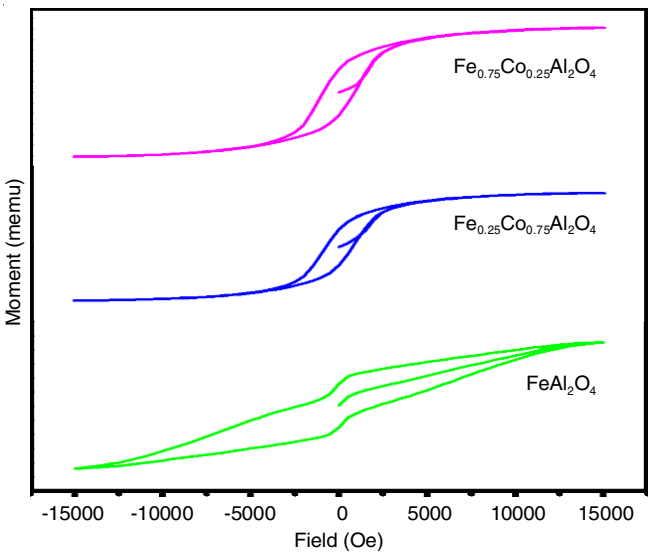

Fig. 6. VSM analysis of ferrite magnetic materials, (a) Pure ($FeAl_2O_4$); (b) excess cobalt ($Fe_{0.25}Co_{0.75}Al_2O_4$) and (c) cobalt deficiency ($Fe_{0.75}Co_{0.25}Al_2O_4$)

at the same applied magnetic field (5 kOe) as listed in Table-2. The pure, cobalt excess and cobalt deficiency ferrite nanoparticles of coercivity decreased from 2212 Oe to 775.45 Oe whereas a considerable increase in saturation magnetization from 4.820×10^{-3} emu/g to 0.673 emu/g was observed. The coercivity for FA-ferrite sample (pure) was found to be 2212.8 Oe, which has been decreased by cobalt excess or cobalt deficiency incorporated Co^{2+} mixed ferrite as observed because of coercivity is inversely proportional to the saturation magnetization ($H_c = K/M_s \times 0.96$). Coercivity was found to have a maximum value of 889.94 Oe [5], indicating that any variation in coercivity was due to factors such as thermal effects, K (3.418 J/m^3 $\longleftrightarrow$ 177.57 J/m^3 $\longleftrightarrow$ 97 J/m^3) and MS values with temperature and particle size. An increase in anisotropy was observed as the particle size decreased, while a decrease occurred when applied magnetic fields were increased. Cobalt excess or cobalt deficiency in $FeAl_2O_4$ may reduce the (Fe^{2+} $\longleftrightarrow$ Co^{2+}) interaction, raising the magnetic moment in the compounds (2.108×10^{-2} and 9.594×10^{-3} Tesla) [6-8]. Its coercivity is also relatively high, at about 889.94. This means that it is difficult to demagnetize the material, making it suitable for use in permanent magnets. The curie temperature of FCA and FCOA is around 860 ºC, which is higher than that of pure iron. This makes it suitable for use in applications that require high temperature stability [2,5,25]. Additionally, the material has a high anisotropy field, which makes it suitable for use in applications that require high magnetic field stability.

Conclusion

Polyvinyl pyrrolidone (PVP) coated cobalt excess and cobalt deficiency employed aluminium ferrite nanoparticles were synthesized by chemical co-precipitation method at 1000 ºC. The average crystallite size of synthesized materials was found to be 17 nm. The smaller crystallite size of the material increases its coercivity, while decreasing its saturation magnetization. VSM analysis indicates that $FeAl_2O_4$ has a normal spinel structure, while $Fe_{0.25}Co_{0.75}Al_2O_4$ and $Fe_{0.75}Co_{0.25}Al_2O_4$ have an inverse spinel structure. Aluminium cobalt ferrites have high coercivity because of their high coercivity value and their low magnetic remanence. This makes them ideal for use in magnetic recording media and permanent magnets because it allows for better storage and magnetization, respectively. Additionally, the high coercivity ensures that the magnets or recordings stay in place and are not demagnetized over time, making them more reliable and longer-lasting.

ACKNOWLEDGEMENTS

The authors thank St. Joseph's College of Arts and Science (Autonomous) for providing the research and library facilities.

CONFLICT OF INTEREST

The authors declare that there is no conflict of interests regarding the publication of this article.

REFERENCES

1. R. Sagayaraj, S. Aravazhi, P. Praveen and G. Chandrasekaran, *J. Mater. Sci. Mater. Electron.*, **29**, 2151 (2018); https://doi.org/10.1007/s10854-017-8127-4
2. T.M. Ali, S.M. Ismail, S.F. Mansour, M.A. Abdo and M. Yehia, *J. Mater. Sci. Mater. Electron.*, **32**, 3092 (2021); https://doi.org/10.1007/s10854-020-05059-y
3. K.M. Tyner, N. Zheng, S. Choi, X. Xu, P. Zou, W. Jiang, C. Guo and C.N. Cruz, *AAPS J.*, **19**, 1071 (2017); https://doi.org/10.1208/s12248-017-0084-6
4. T. Gebel, R. Marchan and J.G. Hengstler, *Arch. Toxicol.*, **87**, 2057 (2013); https://doi.org/10.1007/s00204-013-1158-6
5. R. Sagayaraj, S. Aravazhi, C. Selva kumar, S. Senthil kumar and G. Chandrasekaran, *SN Appl. Sci.*, **1**, 271 (2019); https://doi.org/10.1007/s42452-019-0244-7
6. R. Sagayaraj, M. Jegadheeswari, S. Aravazhi, G. Chandrasekaran and A. Dhanalakshmi, *Chemistry Africa*, **3**, 955 (2020); https://doi.org/10.1007/s42250-020-00153-4
7. R. Sagayaraj, T. Dhineshkumar, A. Prakash, S. Aravazhi, D. Jayarajan, G. Chandrasekaran and S. Sebastian, *Chem. Phys. Lett.*, **759**, 137944 (2020); https://doi.org/10.1016/j.cplett.2020.137944
8. R. Sagayaraj, S. Aravazhi and G. Chandrasekaran, *Int. Nano Lett.*, **11**, 307 (2021); https://doi.org/10.1007/s40089-021-00343-z

9. R. Sagayaraj, *Int. Nano Lett.*, **12**, 345 (2022); https://doi.org/10.1007/s40089-022-00368-y
10. L. Phor, S. Chahal and V. Kumar, *J. Adv. Ceram.*, **9**, 576 (2020); https://doi.org/10.1007/s40145-020-0396-3
11. R.J. Hill, J.R. Craig and G.V. Gibbs, *Phys. Chem. Miner.*, **4**, 317 (1979); https://doi.org/10.1007/BF00307535
12. G.A. Sawatzky, F. Van Der Woude and A.H. Morrish, *Phys. Rev.*, **187**, 747 (1969); https://doi.org/10.1103/PhysRev.187.747
13. T. Sato, K. Haneda, M. Seki and T. Iijima, *Appl. Phys., A Solids Surf.*, **50**, 13 (1990); https://doi.org/10.1007/BF00323947
14. S. Wells and C.V. Ramana, *Ceram. Int.*, **39**, 9549 (2013); https://doi.org/10.1016/j.ceramint.2013.05.073
15. S.S. More, R.H. Kadam, A.B. Kadam, A.R. Shite, D.R. Mane and K.M. Jadhav, *J. Alloys Compd.*, **502**, 477 (2010); https://doi.org/10.1016/j.jallcom.2010.04.201
16. P.S. Aghav, V.N. Dhage, M.L. Mane, D.R. Shengule, R.G. Dorik and K.M. Jadhav, *Physica B*, **406**, 4350 (2011); https://doi.org/10.1016/j.physb.2011.08.066
17. A.I. Borhan, A.R. Iordan and M.N. Palamaru, *Mater. Res. Bull.*, **48**, 2549 (2013); https://doi.org/10.1016/j.materresbull.2013.03.012
18. M. Yehia, S.M. Ismail and M.B. Mohamed, *J. Supercond. Nov. Magn.*, **28**, 3335 (2015); https://doi.org/10.1007/s10948-015-3162-y
19. Y. Dong, H. Lu, J. Cui, D. Yan, F.X. Yin and D.Y. Li, *Ceram. Int.*, **43**, 16094 (2017); https://doi.org/10.1016/j.ceramint.2017.08.142
20. O. Karaagac, B.B. Yildiz and H. Kockar, *J. Magn. Magn. Mater.*, **473**, 262 (2019); https://doi.org/10.1016/j.jmmm.2018.10.063
21. O. Karaagac and H. Kockar, *IEEE Trans. Magn.*, **48**, 1532 (2012); https://doi.org/10.1109/TMAG.2011.2173313
22. T.K. Sau and A.L. Rogach, Complex-Shaped Metal Nanoparticles Wiley-VCH Verlag & Co., KGaA, Weinheim (2012).
23. Z. Alborzi, A. Hassanzadeh and M.M. Golzan, *Int. J. Nanosci. Nanotechnol*., **8**, 93 (2012).
24. R. Sagayaraj, S. Aravazhi and G. Chandrasekaran, *J. Inorg. Organomet. Polym. Mater.*, **29**, 2252 (2019); https://doi.org/10.1007/s10904-019-01183-3
25. R. Sagayaraj, S. Aravazhi and G. Chandrasekaran, *Appl. Phys., A Mater. Sci. Process.*, **127**, 502 (2021); https://doi.org/10.1007/s00339-021-04653-z
26. A. Prakash, R. Sagayaraj, D. Jayarajan, S. Aravazhi, G. Chandrasekaran and R. Nithya, *Asian J. Chem.*, **34**, 2288 (2022); https://doi.org/10.14233/ajchem.2022.23840
27. D.S. Mathew and R.S. Juang, *Chem. Eng. J.*, **129**, 51 (2007); https://doi.org/10.1016/j.cej.2006.11.001
28. N. Abbas, N. Rubab, N. Sadiq, S. Manzoor, M.I. Khan, J. Fernandez Garcia, I. Barbosa Aragao, M. Tariq, Z. Akhtar and G. Yasmin, *Water*, **12**, 2285 (2020); https://doi.org/10.3390/w12082285
29. R.S. Yadav, I. Kuritka, J. Vilcakova, J. Havlica, J. Masilko, L. Kalina, J. Tkacz, J. Švec, V. Enev and M. Hajdúchová, *Adv. Nat. Sci.: Nanosci. Nanotechnol.*, **8**, 045002 (2017); https://doi.org/10.1088/2043-6254/aa853a
30. W. Gu, Q. Xie, M. Xing and D. Wu, *Chem. Eng. Res. Des.*, **117**, 706 (2017); https://doi.org/10.1016/j.cherd.2016.11.026
31. C. Murugesan and G. Chandrasekaran, *RSC Adv.*, **5**, 73714 (2015); https://doi.org/10.1039/C5RA14351A
32. A. Ashok, L.J. Kennedy and J.J. Vijaya, *J. Alloys Compd.*, **780**, 816 (2019); https://doi.org/10.1016/j.jallcom.2018.11.390
33. S.A. Al-Zahrani, A. Manikandan, K. Thanrasu, A. Dinesh, K.K. Raja, M.A. Almessiere, Y. Slimani, A. Baykal, S. Bhuminathan, S.R. Jayesh, J. Ahmed, H.S. Alorfi, M.A. Hussein, I. Khan and A. Khan, *Crystals*, **12**, 268 (2022); https://doi.org/10.3390/cryst12020268
34. M.Y. Lodhi, K. Mahmood, A. Mahmood, H. Malik, M.F. Warsi, I. Shakir, M. Asghar and M.A. Khan, *Curr. Appl. Phys.*, **14**, 716 (2014); https://doi.org/10.1016/j.cap.2014.02.021
35. J. Fukushima, Y. Hayashi and H. Takizawa, *J. Asian Ceramic Soc.*, **1**, 41 (2013); https://doi.org/10.1016/j.jascer.2013.02.001
36. D.P. Dutta and G. Sharma, *Mater. Sci. Eng. B*, **176**, 177 (2011); https://doi.org/10.1016/j.mseb.2010.10.018
37. X. Duan, M. Pan, F. Yu and D. Yuan, *J. Alloys Compd.*, **509**, 1079 (2011); https://doi.org/10.1016/j.jallcom.2010.09.199
38. A. Walsh, S.-H. Wei, Y. Yan, M.M. Al-Jassim, J.A. Turner, M. Woodhouse and B.A. Parkinson, *Phys. Rev. B Condens. Matter Mater. Phys.*, **76**, 165119 (2007); https://doi.org/10.1103/PhysRevB.76.165119
39. T.P. Yadav, N.K. Mukhopadhyay, R.S. Tiwari and O.N. Srivastava, *J. Nanosci. Nanotechnol.*, **7**, 575 (2007); https://doi.org/10.1166/jnn.2007.128